Liquid Metal-Based Flexible Sensor for Perception of Force Magnitude, Location, and Contacting Orientation

Min Wang, *Graduate Student Member, IEEE*, Jingjing Zhang, Ruomao Liu, Tianyi Wu, Wei Dai, Rui Liu, Jiachen Zhang, *Member, IEEE*, and Jun Liu, *Member, IEEE*

***Abstract*— Flexible sensors have the advantage to enable intelligent systems to interact with the environment with high safety and versatility. Liquid metal is a useful element for flexible sensors due to its stretchable, reconfigurable, and healing characteristics. However, it is difficult to decode the stimuli position using uniform liquid metal because of its homogeneity and fluidity. Current sensing systems for the perception of force magnitude and contact location mostly rely on sensing arrays and massive crossover electrodes. In this article, we proposed a novel method for simultaneously sensing the force magnitude and contact location without crossover electrodes. In the new design, we encapsulate the liquid metal electrodes with varying cross sections in two silicon layers that function as protective skin and govern the geometry of liquid metals. When a force is applied to the flexible sensor, the change of resistance is dependent on both location and stimuli magnitude. Three liquid metal channels with different gradient resistance are embedded in the prototypes with parallel distributions. Combining the signals collected from the three channels, we can simultaneously measure the force magnitude, stimuli location, and contacting orientation. The overall force resolution is sub-Newton in the range from 0.5 to 20 N. The position can also be determined with a 100% success rate for the segmented sensor and a position resolution of 2 mm for the continuous sensor. The error for contact orientation measurement is 4.58° when the orientation ranges from 45° to 135°. The proposed multifunctional sensing device with high accuracy and wide sensing range has significant potential for developing interactive interfaces for human–machine interactions and industrial applications.**

***Index Terms*— Flexible sensors, force decouple, intelligent systems, multifunctional perception, soft robotics.**

Manuscript received 5 December 2022; revised 13 March 2023; accepted 18 March 2023. Date of publication 10 April 2023; date of current version 26 April 2023. This work was supported in part by the Research Grant Council (RGC) of Hong Kong under Grant 11212321, Grant 11217922, and Grant ECS-21212720; in part by the Basic and Applied Basic Research Foundation of Guangdong Province Fund Project under Grant 2019A1515110175; in part by the Science, Technology and Innovation Committee of Shenzhen under Grant SGDX20210823104001011; and in part by the Zhejiang Laboratory International Talent Fund for Young Professionals. The Associate Editor coordinating the review process was Dr. Anoop Chandrika Sreekantan. *(Corresponding author: Jun Liu.)*

Min Wang, Jingjing Zhang, Tianyi Wu, Wei Dai, Rui Liu, and Jun Liu are with the Department of Mechanical Engineering, City University of Hong Kong, Hong Kong, SAR, China(e-mail: jun.liu@cityu.edu.hk).

Ruomao Liu and Jiachen Zhang are with the Department of Biomedical Engineering, City University of Hong Kong, Hong Kong, SAR, China.

Digital Object Identifier 10.1109/TIM.2023.3265759

I. Introduction

FLEXIBLE sensing techniques have shown significant value in a wide range of applications, including wearable devices, artificial skin, soft robotics, and health monitoring systems [1], [2], [3], [4]. Compared with traditional rigid transducers, flexible sensors have the intrinsic advantages of high compliance with irregular surfaces, high durability, and stability [5]. For example, rigid sensors are more likely to be damaged by unexpected mechanical stimuli, resulting in decreased sensitivity or breakdown of the devices. In comparison, flexible sensors made of soft materials can recover to the initial state when the external stimuli are released. In addition, a large array of rigid sensing units is required for large planar sensing, whereas several compliant sensors can implement localization and measurement of external stimuli with well-designed structures made of soft materials, for example, sinusoidally magnetized polymer films [6] and distinct magnetization directions in adjacent regions [7]. The unique features of soft sensors enable interaction with surroundings with more information and a higher level of compliance than conventional rigid sensors [8].

Various sensing principles have been applied to the development of flexible tactile sensors, including resistive [9], [10], capacitive [11], piezoelectric [12], triboelectric [13], and magnetic force sensing [14], [15]. Among these sensing principles, piezoresistive materials have been widely used because of their low costs and high reliability. Moreover, other characteristics of the piezoresistive sensor, including wide measuring range, high accuracy, and simple structure, also contribute to the wide applications in the measurement of pressure [5], [16], torque [17], and acceleration [18].

Flexible sensors based on resistive sensing are mainly composed of conductive electrodes embedded in flexible structures. Various materials, such as carbon particles [19], silver nanowires [20], conductive polymers [21], and liquid metals [22], [23], [24], have been used as conductive electrodes. Among them, liquid metal has emerged as a superior choice because of its unique properties of being conformable, reconfigurable, highly conductive, and self-healing. To fabricate liquid metal sensors, Ren et al. [25] proposed a spraying-and-wiping process to fabricate high-resolution circuits (i.e., 50 um) to characterize bending and stretching.

1557-9662 © 2023 IEEE. Personal use is permitted, but republication/redistribution requires IEEE permission.
See https://www.ieee.org/publications/rights/index.html for more information.

Authorized licensed use limited to: The University of Hong Kong Libraries. Downloaded on October 05,2024 at 12:00:07 UTC from IEEE Xplore. Restrictions apply.

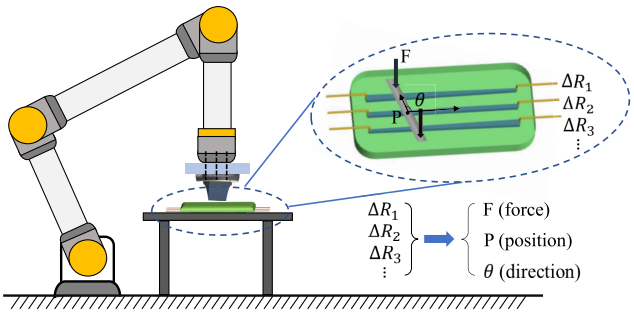

Fig. 1. Overview diagram of perception force magnitude, contact position, and orientation.

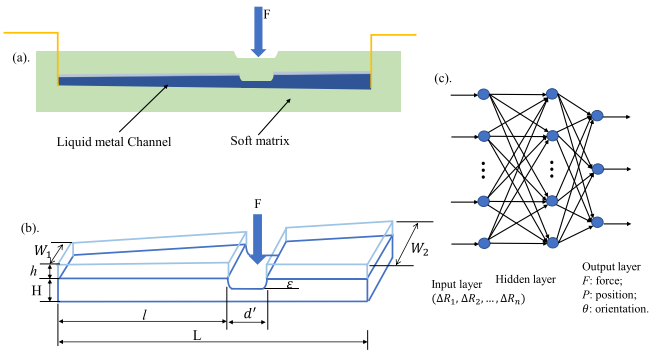

Fig. 2. Sensing principle of the proposed sensor. (a) Schematic shows the side view of the liquid metal-based sensor. The applied force deforms the channel and increases the overall resistance. (b) 3-D perspective view shows the trapezoidal cylinder geometry produces a continuous gradient of resistance when filled with liquid metal. (c) Neural network is used to calculate the applied force, contact position, and orientation by measuring the resistance values from multiple liquid metal channels.

For multifunctional perception, Wang et al. [26] developed a wearable sensor for the simultaneous measurement of temperature and contact force. Liquid metal-based flexible sensors were also developed for other applications including microfluidic pressure monitoring [27], continuous intraocular pressure monitoring [28], and magnetic field detection [29].

Accurate perception of force and contact location is critical for many robotic applications (e.g., grasping irregular objects). Recent publications have reported a force decoding system with three electrical paths and eight segments to measure the force and position simultaneously [30]. The segments along each electrical path have distinct sensitivity to determine the force magnitude and recognize the applied location. Similarly, Wei et al. [31] proposed a carbon-based sensor with a gradient resistance to achieve multipoint tactile sensing. Nevertheless, the two methods can only differentiate the forces into segmented regions rather than continuous areas. Yang et al. [32] developed an addressable force sensing method by using two layers of capacitive sensors with slant dielectric layers. However, this method requires multiple layers of the capacitor to achieve 2-D position and force perception in a higher resolution.

To address the limitations mentioned above, we propose a new liquid metal-based flexible sensor with continuous gradient resistance for the simultaneous measurement of force and touch positions. As shown in Fig. 1, three trapezoidal liquid metal channels are embedded in parallel in the silicon substrate. Because of the anisotropic cross section, the proposed sensor has a changing sensitivity in the longitude direction. When a force is applied to the flexible sensor, the changed resistances in the three channels are different. The measured resistance values from various channels are fed to a neural network model to determine both the intensity and applied location of the external stimulus. Moreover, the position measurement from different channels can be used to determine the touching orientations. As a result, the external stimuli applied at different positions and orientations are decoded by analyzing the resistance change from various channels.

The novelty of the presented sensor includes: 1) an absolute force decoder that can decouple the external stimuli to force amplitude, position, and orientation; 2) a liquid metal-based sensor with a continuous gradient of resistance that can achieve continuous sensing with high precision; and 3) a simple structure of parallel channels that can eliminate the massive crossover electrodes, signal crosstalk, and demanding configurations.

II. Mechanism

Nature organisms can convert external physical stimuli (e.g., mechanical force, pressure, and heat) into biological signals that the brain can recognize. In addition to sensing the stimulus intensity, the organism can also determine the position where the stimulus is applied. Inspired by the multifunctional sensing mechanism in natural organisms, we propose a new design of a flexible sensor embedded with liquid metal for tactile sensing. The liquid metal used in this article is the eutectic gallium–indium–tin alloy with the composite of 68.5 wt% gallium, 21.5 wt% indium, and 10 wt% tin. The melting point of the liquid metal is 11 °C ensuring a liquid state under room temperature. Due to the high electrical conductivity and deformability, liquid metal is a promising material for converting mechanical signals into a change of resistance. We designed the liquid metal channels with a varied cross section to enable the sensor the capability of position recognition. As shown in Fig. 2(a), the liquid metal channel is sandwiched between two silicon layers that act as a protective skin to maintain the initial geometry of liquid metal channels.

According to the law of resistance: $R = \rho L/A$, when the sensor is subjected to external mechanical stimuli (e.g., pressure, thermal expansion, or stretching), the resistor made of liquid metal deforms with a changing cross section, and the resistance changes accordingly. We can choose the conductive filament with varied resistivity (ρ) or edit the geometry of the resistor to enable the sensor with a gradient resistance. Here, we designed a liquid metal channel with a gradually increased cross sectional area, as shown in Fig. 2(b). When no external force is applied, the liquid metal fills the entire trapezoidal channel, and the total resistance is

$$R = \int_0^L \rho \frac{1}{\left[W_1 + \left(\frac{W_2 - W_1}{L}\right) l\right] H} dl \tag{1}$$

Authorized licensed use limited to: The University of Hong Kong Libraries. Downloaded on October 05,2024 at 12:00:07 UTC from IEEE Xplore. Restrictions apply.

where L is the total length of the liquid metal channel, ρ is the resistivity of liquid metal, W_1 is the width of the narrowest cross section, W_2 is the width of the broadest cross section, and H is the height of the channel.

When an external force is applied to the sensor, the contact area deforms and reduces the area of the cross section [Fig. 2(b)]. Accordingly, the overall resistance is increased with the external force. In this study, we use a 3-D-printed bar with a width of d to press the soft sensor. We regard the sensor as a uniform elastomer by neglecting the influence of liquid metal channels on the elastic modulus of the elastomer and the internal damping of the elastomer. According to Hooke's Law, $\varepsilon = F/E$, the deformation of the liquid metal channel is proportional to the mechanical force F and related to Yang's module E of the soft matrix. Since the touching width d is much smaller than the total length of liquid metal channel L, the contact area on the top surface can be approximated to a rectangle instead of a trapezoid for simplicity. The corresponding increment of resistance at the touching position is

$$\Delta R_{\text{in}} = \frac{\rho d'}{\left(H - \frac{F}{E}\right)\left(W_1 + \frac{W_2 - W_1}{L} l\right)} - \frac{\rho d}{H\left(W_1 + \frac{W_2 - W_1}{L} l\right)} \quad (2)$$

where d' is the contact portion of the liquid metal channel, which is slightly wider than the stick width d. For simplicity of discussion, d' is expressed as d in the following part since the stretch value $(d' - d)/d$ is small. From the equation, we can find that ΔR_{in} will increase with the applied force F, and the trend of increasing is nonlinear as the geometry changes are reflected in the denominator of the first term. The liquid metal within the compressed area is pushed by the applied forces and flows to the surrounding area. Theoretically, the liquid metal will be uniformly distributed in the uncompressed channel. The redistribution of the liquid metal results in the increased height of the liquid metal can be regarded as follows:

$$h = 2\frac{Fd[LW_1 + (W_2 - W_1)l]}{E(W_1 + W_2)L^2}. \quad (3)$$

The diminution of corresponding resistance can be expressed as follows:

$$\Delta R_{\text{di}} = \int_0^L \rho \frac{1}{\left[W_1 + \left(\frac{W_2 - W_1}{L}\right)l\right](h + H)} dl - \int_0^L \rho \frac{1}{\left[W_1 + \left(\frac{W_2 - W_1}{L}\right)l\right]H} dl. \quad (4)$$

Combining (2) and (4), we can obtain the changed resistance of a channel when the external force is applied to the soft sensor

$$\Delta R = \Delta R_{\text{in}} + \Delta R_{\text{di}}. \quad (5)$$

The change of resistance is related not only to the magnitude of the applied force [reflected as the displacement (ε)], but also to the position where the force is applied (l). Although approximation errors exist in the analytical model of the resistance change due to the simplification of mechanics, trained neural networks are powerful tools to understand and solve the complexity of the physics between the resistance and applied forces as well as pressing positions.

For simplicity, we can express the change of resistance ΔR as a function of force and contacting position

$$\Delta R = f(F, P) \quad (6)$$

where F is the magnitude of applied force and P represents the contacting position.

According to (6), the change of resistance is related to both the applied force F and the contact position P. We can obtain the solution of applied force and contact position when there are more than two channels. No matter which channel has a larger ΔR, it will not influence the solution of F and P, as long as we can ensure a unique changing trend of resistance in different channels. Implementation of multiple channels with different geometries can further increase the measurement performance to obtain numerical solutions or optimization results.

As shown in Fig. 2(c), the signals collected from multiple channels were fed to a neural network to calculate the final force amplitude and touched position. Moreover, contact orientation can also be measured by connecting the contact points on different channels. The back-propagation neural network was adopted in this article because of its wide employment and exemplary performance in soft sensor systems [32], [33], [34], [35].

III. Design and Fabrication

In this study, we designed two prototypes, one with continuously varying cross sections and the other with segmented varying cross sections. Both prototypes are integrated with three channels to allow for the simultaneous measurement of force magnitude, contacting position, and contacting orientation. The fabrication methods are the same for both prototypes except for the variations in mold manufacturing. In this section, we use the liquid metal sensor with a continuously varied cross section to introduce the fabrication process (see Fig. 3).

In the first step, we fabricated two molds by 3-D printing polylactic acid (PLA) with a commercial 3-D printer. The first mold has a depth of 4 mm and three raised ridges with a height of 2 mm. The three ridges are used to form the liquid metal channels. The second mold is 6 mm in depth without any raised ridges. After that, we prepared silicone polymers ecoflex00-30 by mixing and stirring parts A and B agents with a ratio of 1:1. The mixed part is then poured into the mold after 10 min of degassing. After curing for four hours at room temperature, the silicone base is peeled off and put in a deeper mold in a reverse direction. In the next two steps (i.e., steps 4 and 5), we poured the melted wax to fill the channels and then scraped off the excess wax overflowing on the surface with a scraper. We then covered the wax-filled base with another layer of ecoflex00-30 at a thickness of 2 mm in step 6. After the silicon rubber was cured, we perforated the end of each wax channel to remove the wax and inject the liquid metal. The silicon rubber embedded with wax is then placed on a hot plate for melting and draining the wax. In the last step, we injected the liquid metal into the three channels and inserted copper wires at both ends, followed by a sealing process using uncured ecoflex00-30.

Authorized licensed use limited to: The University of Hong Kong Libraries. Downloaded on October 05,2024 at 12:00:07 UTC from IEEE Xplore. Restrictions apply.

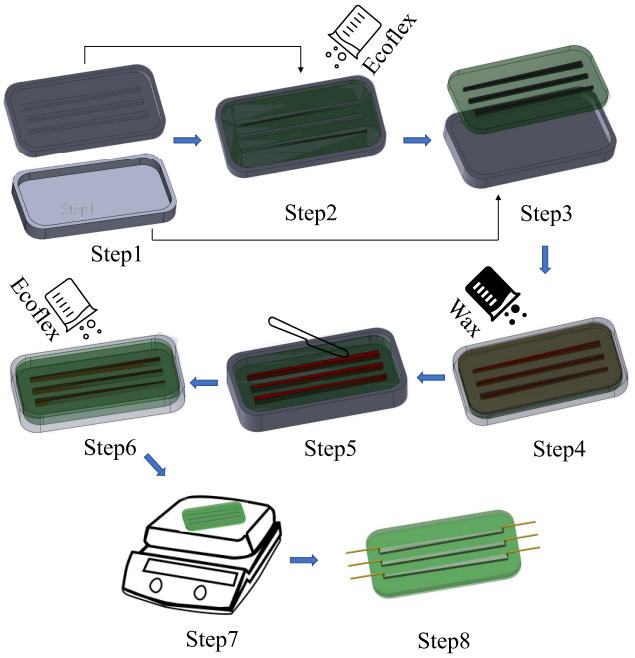

Fig. 3. Illustration of the fabrication process of the flexible sensor comprising multiple channels with continuous gradient geometry.

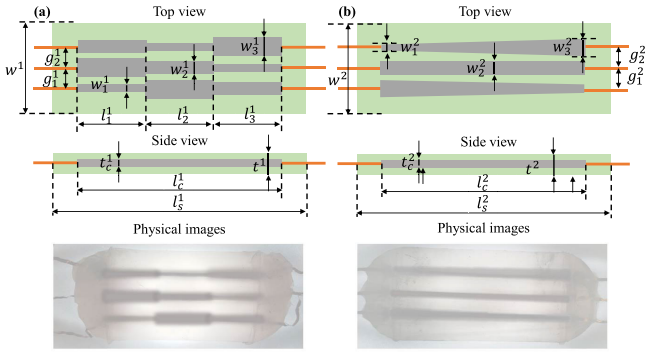

Fig. 4. Structure and fabrication results of two proposed force-decoding sensors; green: soft matrix, gray: liquid metal. (a) Segmented gradient resistance sensor. (b) Continuous gradient resistance sensor.

The design structure and final fabrication results of two flexible sensors are shown in Fig. 4. The overall size of the flexible sensor is 90 × 40 mm with a thickness of 6 mm. The liquid metal channels with a thickness of 2 mm are embedded in the middle of the silicone matrix. For the segmented flexible sensor, the widths of the liquid metal in the same channel vary across the three segments at different values of 1.8, 2.5, and 3.0 mm, respectively. In the same segment, we kept the width of the three channels different from each other by switching the orders. In the continuous design, the width of the first channel [i.e., the top channel in Fig. 4(b)] increases gradually from 1.8 to 3.0 mm, while the third channel [i.e., the bottom channel in Fig 4(b)] decreases from 3.0 to 1.8 mm. The middle channel remains at a constant width of 2.5 mm. The gap between two adjacent liquid metal channels is 10 mm. More detailed parameters are listed in Table I.

IV. Experiments and Results

In this study, we designed new flexible sensors that can measure the magnitude and position of external stimuli simultaneously. When the flexible sensor is pressed, the geometry of the liquid metal-filled channel changes, resulting in a change of resistance. Because of the anisotropic cross section, the resistance change is different when the same force is applied to different positions. The schematic of the experimental setup is shown in Fig. 5(a). The robotic arm (xmate7pro, ROKAE Company Ltd.) is used for changing the position and orientation of applied force. A load cell (HZC-T 0-50N with an accuracy of 0.05%.) mounted on the end-effector ensures well-controlled forces with known magnitudes. A customized contacting stick is used to touch and deform the flexible sensor.

The real-time resistance values in the three channels are measured by an eight-channel resistance meter (AT5108, Anbai Company Ltd.). The measuring range is from 1 $\mu\Omega$ to 30 kΩ with an accuracy of 0.05%. The scan time for each channel is about 30 ms, which is acceptable for most stimuli situations of real-time monitoring. The measured resistance is then uploaded to the host computer via a serial portal.

TABLE I
Parameters and Related Values of the Proposed Flexible Sensors

Segmented prototype		Continuous prototype	
Parameter	Values (mm)	Parameter	Values (mm)
l_s^1	90	l_s^2	90
l_c^1	75	l_c^2	75
w^1	40	w^2	40
w_1^1,	1.8	w_1^2	1.8
w_2^1,	2.5	w_2^2	2.5
w_2^1,	3.0	w_2^2	3.0
t_c^1,	2.0	t_c^2	2.0
t^1,	6.0	t^2	6.0
g_1^1, g_2^1	10	g_1^2, g_2^2	10
l_1^1, l_2^1 , l_3^1	25		

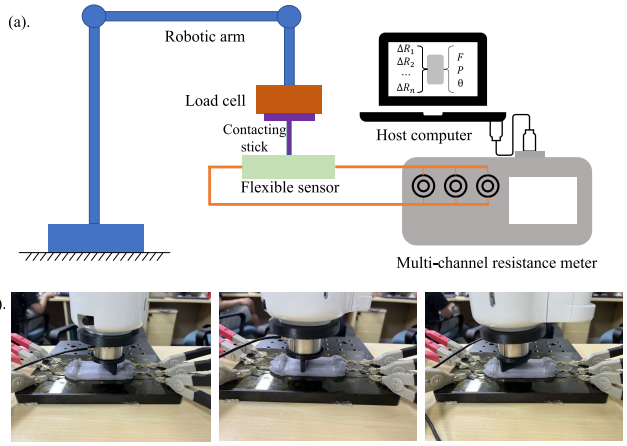

Fig. 5. Experimental design and testing of the flexible sensors. (a) Schematic shows that the resistance of several channels is measured by a multichannel resistance meter and then uploaded to a host computer. (b) Physical images show the flexible sensor is being tested by applying a given force at different positions and orientations from a robotic arm and load cell.

Authorized licensed use limited to: The University of Hong Kong Libraries. Downloaded on October 05,2024 at 12:00:07 UTC from IEEE Xplore. Restrictions apply.

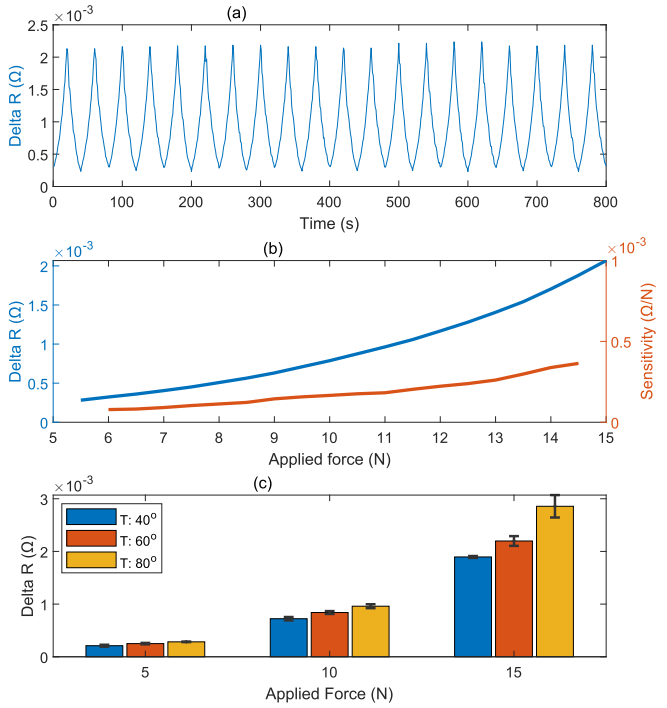

Fig. 6. Characterization of the proposed sensor. (a) Verification of the repeatability. (b) Test of the sensitivity. (c) Effect of temperature on sensor performance.

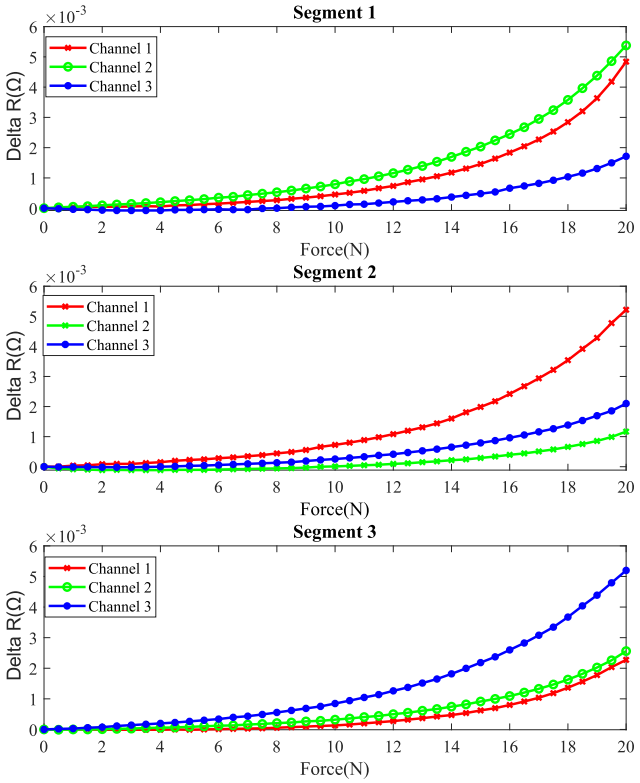

Fig. 7. Change of resistance versus applied force from 0 to 20 N for different channels. The first figure shows $\Delta R_2 > \Delta R_1 > \Delta R_3$ or force from 0 to 20 N, corresponding to the channel width variations from large to small. While $\Delta R_1 > \Delta R_3 > \Delta R_2$ or the second figure, $\Delta R_3 > \Delta R_2 > \Delta R_1$ or the third figure.

Finally, our AI-based algorithm processes the resistance values and decouples the force magnitude, contacting position, and orientation. Fig. 5(b) shows the physical images when the robotic arm touches the flexible sensor at different positions and orientations.

We evaluated the repeatability of the proposed sensor by repeating the pressing process 20 times on a liquid metal channel with a width of 1.8 mm. The applied force was increased from 5.5 to 15 N and then released to 5.5 N with a step of 0.5 N. The experimental results in Fig. 6(a) show that the proposed sensor has high repeatability to external press force. The recorded resistance values were then averaged and plotted in Fig. 6(b) (blue line). The calculated sensitivity of the proposed sensor [Fig. 6(b) (red line)], ranging from 7.8×10^{-2} to 3.64×10^{-1} mΩ/N, is increased with the applied force.

We tested the effect of temperature on sensor performance. The results [Fig. 6(c)] show that a higher temperature can result in a more sensitive response. The results indicate that a recalibration process is required when the sensor is deployed to a high-temperature environment. To test the robustness of the sensor under conditions, we recorded the sensor's response in the dry and wet tanks, and on a PZT vibration plate with different voltage inputs (1–12 V). The output of the sensor remains stable with a deviation of lower than 4.8% and 5.4%, respectively.

A. Segmented Position and Force Perception

To evaluate the performance of the segmented flexible sensor, we applied forces ranging from 0 to 20 N with an interval of 0.5 N on different segments. The change of resistance, reflected as the difference between the real-time resistance value and the rest state value, under different stimuli is shown in Fig. 7. Three subfigures show the performance of changed resistance on segmentation 1, 2, and 3, respectively. The resistance value varies for all three channels when the stimuli force is raised. However, the changing rates are different for the three channels. More specifically, the resistance increases dramatically when the cross section area is narrow, indicating a nonlinearly increase between the resistance value and the applied force. Because the flexible sensor has varied cross sections for the three channels [shown in Fig. 4(a)], we can quickly recognize the stimuli' segments by comparing the changed resistance of the three channels. For example, for segmentation 1, we can always find that $\Delta R_1 > \Delta R_2 > \Delta R_3$ for different stimuli magnitude.

To evaluate the force recognition accuracy of the proposed flexible sensor and our algorithms, we repeated the experiment 15 times with the force from 0.5 to 20 N at three segments and recorded the resistance value of the three channels. We also recorded the applied force and the contact position simultaneously. The total recorded 1800 sets of data are randomly divided into three groups, where 70% were used for training a BP network, and the remaining 30% was divided equally for validation and testing. To evaluate the quality of the training model, we define the prediction error as follows:

$$\text{Error} = \frac{1}{n}\sum_{i=1}^{n} |F_p - F_a| \tag{7}$$

Authorized licensed use limited to: The University of Hong Kong Libraries. Downloaded on October 05,2024 at 12:00:07 UTC from IEEE Xplore. Restrictions apply.

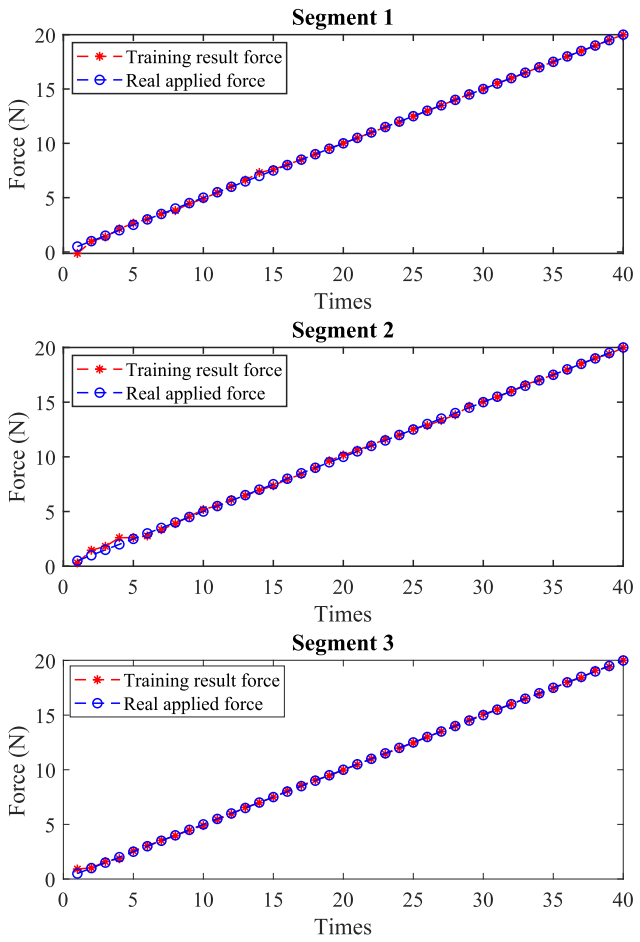

Fig. 8. Comparing the training results and real applied forces. The figure shows a good overlap in the three segments.

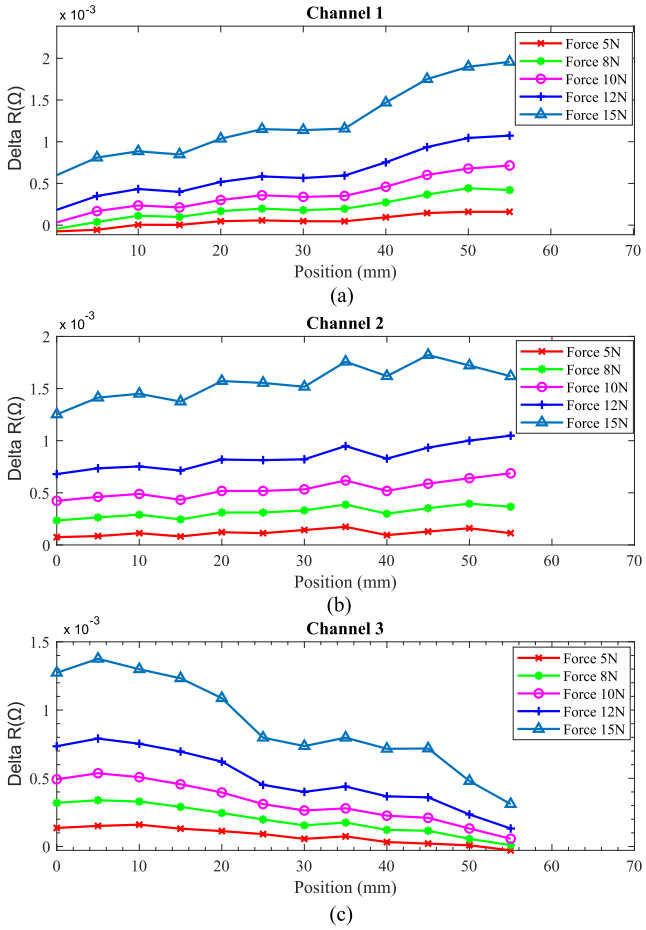

Fig. 9. Change of resistance versus the contact positions under different applied forces. (a) Change of resistance in channel 1 decreases dramatically when the contact position changes from left to right, corresponding to a continuously increased channel width. (b) Resistance changes in channel 2 are relatively stable due to the constant channel width. (c) In contact with channel 1, the change of resistance in channel 3 increases when the channel width decreases from left to right.

where F_p is the predicted force by the trained model, F_a is the applied force recorded by the load cell, and n is the number of contact times.

Fig. 8 compares the predicted force by the neural network and the ground truth of the applied force. We can find that the predicted values at the three segments all overlap well with the true values. The predicted errors of the three segments are 0.051, 0.133, and 0.162 N, respectively.

B. Simultaneous Force and Contact Position Perception

To simultaneously measure the magnitude and location of external forces, we exerted stimuli on different positions of the flexible sensor with force ranges from 5 to 15 N. In this experiment, we change the contact locations from left to the right (i.e., from 0 to 55 mm along the longitudinal axis). The prototype evaluated in this experiment is the continuous design [i.e., the model shown in Fig. 4(b)].

The change in resistance is illustrated in Fig. 9. For each channel, a stronger force stimulation results in a more significant change in the resistance. As for channel 1, the changed resistance, $\triangle R$, decreases from left to right when the same amplitude of force is applied to the sensor. However, the resistance changes of channel 3 exhibit the opposite behavior, that is, the value of the resistance increases from left to right. This phenomenon is due to the fact that the cross section of channel 1 increases from left to right, while channel 3 has a reverse design to decrease the channel width along the longitudinal axis. We can also find that the change of resistance increases more obviously when the contact position approaches the narrow area. The nonlinear increasing trend is due to the higher sensitivity of the smaller cross section of the liquid metal channels.

We designed channel 2 with a uniform pattern, resulting in constant resistance changes among all contact locations [shown in Fig. 9(b)]. The fluctuations of resistance changes in channel 2, especially when a large force is applied, are largely attributed to manufacturing errors. We also find that the change of resistance, ΔR, increases faster when the applied force is greater for all three channels. For example, the gap between the cyan line (Force 15 N) and the blue line (Force 12 N) is much wider than the gap between the green line (Force 8 N) and the red line (Force 5 N). The nonlinear changes are attributed to the fact that when a larger force is pressed, the liquid metal deforms significantly, resulting in a smaller cross section. Accordingly, the sensitivity is much

Authorized licensed use limited to: The University of Hong Kong Libraries. Downloaded on October 05,2024 at 12:00:07 UTC from IEEE Xplore. Restrictions apply.

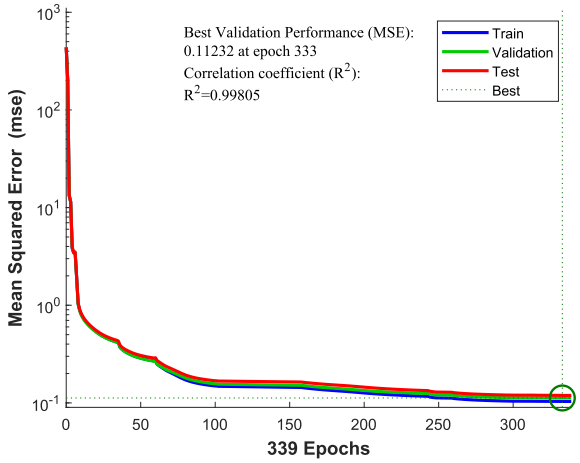

Fig. 10. Training process using the BP neural network.

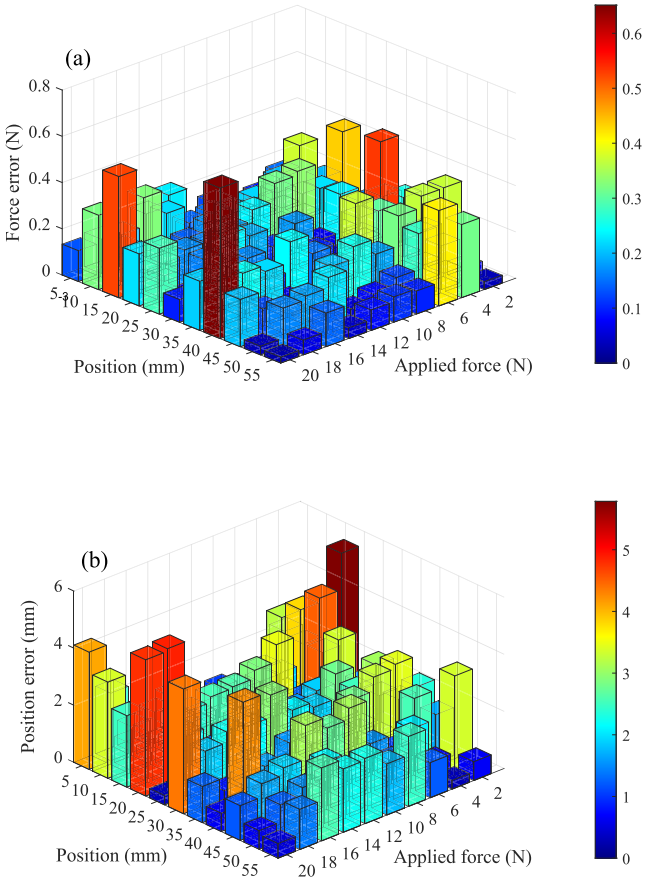

Fig. 11. Average error of simultaneous sensing applied for forces and contact positions. (a) Force error for stimulation with the force of 0–20 N in the range of 50 mm. (b) Position error for stimulation with the force of 0–20 N in the range of 50 mm.

higher when the cross section is smaller for the liquid metal sensor.

To evaluate the accuracy of simultaneous perception of applied force and stimuli position, we tested the flexible sensor from left to right with forces ranging from 0.5 to 20 N 15 times. The resistances of the three channels are recorded and randomly divided into three groups (training, validation, and testing), following the same rules as Section IV-A. Fig. 10 shows the training process, the mean squared error for the validation experiments stabilizes at 0.11232, and the corresponding correlation coefficient R^2 reaches 0.99805 for the dataset, showing good stability and regression accuracy for the neural network. The data was also trained by RBN and SOM neural networks. The corresponding correlation coefficient R shows good fitting behaviors, that is, $R^2 = 0.99752$ and$R^2 = 0.99213$, respectively. The results indicate that the proposed system is robust to different neural networks.

We can obtain the sensing errors by comparing the AI-processed results with the applied forces (recorded by the load cell) and positions (reflected by the robot arm system). As shown in Fig. 11, the sensing accuracy is constantly high for all measured positions. In more detail, the force error is below 0.8 N for all situations and the position error for most states is lower than 4 mm. Interestingly, the sensing errors slightly increase when the applied force within low (e.g., 2 N) or high (e.g., 20 N) levels. The reason is that when a slight force is applied, the minor change of resistance $\triangle R$ is difficult to measure with high accuracy. In addition, the small value of $\triangle R$ also increases the difficulty for the neural network to obtain a high-accuracy result. On the other hand, when a heavy force is applied, the changes in geometry are unstable. Moreover, a heavy force results in a narrow cross section and a higher sensitivity, making the system more susceptible to environmental disturbances (e.g., mechanical vibration, local heat, and so on).

Table II summarizes the accuracy of force and contact position perception at different force ranges. The evaluation results

TABLE II

AVERAGE ERROR AND STANDARD DEVIATION FOR FORCE SENSING AND POSITION RECOGNITION AT DIFFERENT STIMULI FORCE RANGE

Sensing error	Applied force range (N)			
	0 - 5.0	5.5 - 10.0	10.5 - 15.0	15.5 - 20.0
Position (mm)	0.25±0.19	0.16±0.11	0.14±0.08	0.17±0.12
Force (N)	3.40±3.32	1.68±0.93	1.60±0.91	1.87±1.24

are separated into four groups according to the amplitude of the applied forces (i.e., 0.5–5, 5.5–10, 10.5–15, and 15.5–20 N in Table II). It can be observed that both average error and standard deviation in the small force range (i.e., the first column in Table II) are higher than the values in the other three ranges. In addition, there is no significant difference between the ranges in the last three columns, indicating a reliable measurement performance between 5 and 20 N.

C. Simultaneous Force and Contact Orientation Perception

Previous sections evaluated the sensor performance in measuring the applied force amplitude and locations simultaneously. The contacting orientation could be further calculated by connecting the positions on different channels. In this

Authorized licensed use limited to: The University of Hong Kong Libraries. Downloaded on October 05,2024 at 12:00:07 UTC from IEEE Xplore. Restrictions apply.

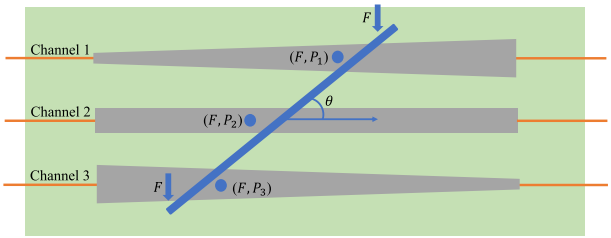

Fig. 12. Diagram of simultaneously applied force and contact orientation sensing using the continuous gradient resistance sensor.

section, we extend the application of the proposed prototype to sense the applied force and pressed orientation simultaneously. As shown in Fig. 12, when a contacting stick touches the flexible sensor in different directions (denoted as θ), the measurement system can accurately measure the different contacting locations on the three channels. We can determine the contacting orientation by connecting the positions of different channels or finding an optimal pressed line with the smallest sum of distances from these points.

In this section, we pressed the flexible sensor in different orientations at five positions with forces ranging from 0.5 to 20 N. The contacting orientations change from 45° to 135° with an integral of 15°, and the distance between contacting positions is 5 mm. The five points from left to right are denoted as P1–P5. A similar BP neural network is built to process the measured resistance and predict the force amplitude and contacting orientations. From left to right, a total of five positions are verified.

The ground truth of contact orientation and stimuli force are obtained from the testing robot arm and the load cell. Comparing the predicted value and the ground truth, Fig. 13 shows the sensing accuracy for force and orientation in five positions. We can find that sensing accuracy at the two ends (i.e., P1 and P5) is higher than that in the middle area (i.e., P2–P4). These variations in accuracy can be attributed to the significant difference in the channel geometry at the two ends. The geometry of the three channels is similar in the middle area, making it difficult for the BP network to differentiate. However, all force errors are lower than 0.6 N, suggesting the prototype and algorithm can produce a high accuracy for force measurement at different contacting positions and orientations.

To compare the sensing accuracy at different contacting positions and evaluate the stability of the flexible sensor. We also plot the average sensing error and standard deviation for the five contact points in Fig. 14. In this figure, both the force errors and the orientation errors of the three positions in the middle are slightly larger than the positions at the two ends.

V. Discussion

With two different configurations (i.e., segmented and continuous gradient channels), we conducted three verification experiments, including section recognition and force sensing, simultaneous position and force sensing, as well as simultaneous force and contract orientation sensing. The overall sensing accuracy for all three experiments is summarized in Table III. The results show that the flexible sensor system can achieve a high resolution in a wide force range.

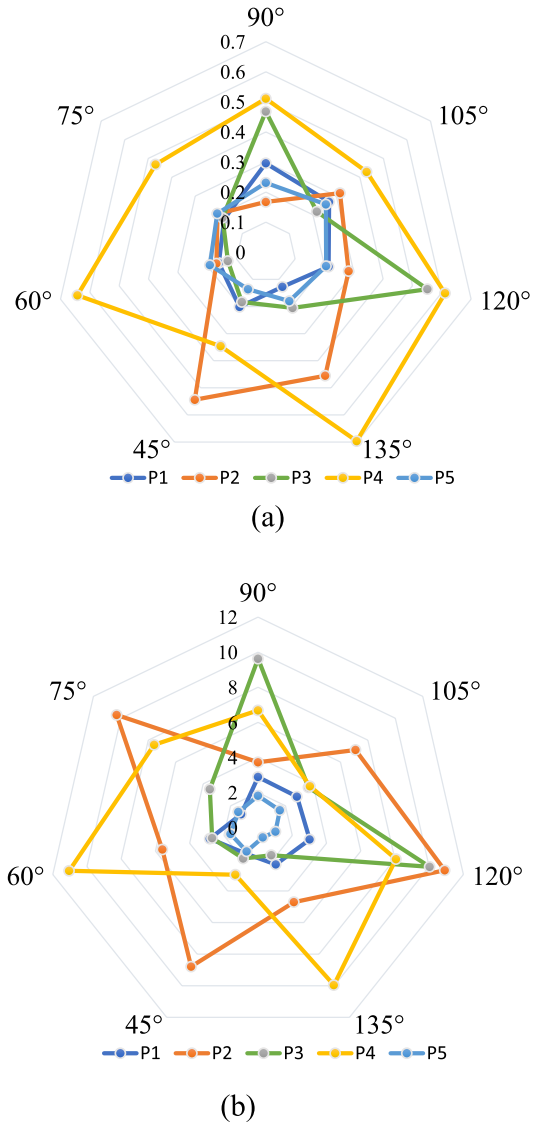

Fig. 13. Average error of simultaneous sensing applied forces and contact orientations. (a) Force error for stimulation with five positions from 5 to 25 mm and orientation from 45° to 135°. (b) Orientation error for stimulation with five positions from 5 to 25 mm and orientation from 45° to 135°.

TABLE III
Sensing Error for Three Sensing Modes. Type I: Segmented Position Recognition and Force Detection. Type II: Simultaneous Sensing of Applied Force and Contact Position. Type III: Simultaneous Sensing of Applied Force and Contact Orientation

Sensing type	Sensing error		
	Magnitude (N)	Position (mm)	Orientation (o)
I	0.077±0.105	0	−−
II	0.219±0.147	2.396±2.460	−−
III	0.249±0.244	−−	4.585±5.908

Authorized licensed use limited to: The University of Hong Kong Libraries. Downloaded on October 05,2024 at 12:00:07 UTC from IEEE Xplore. Restrictions apply.

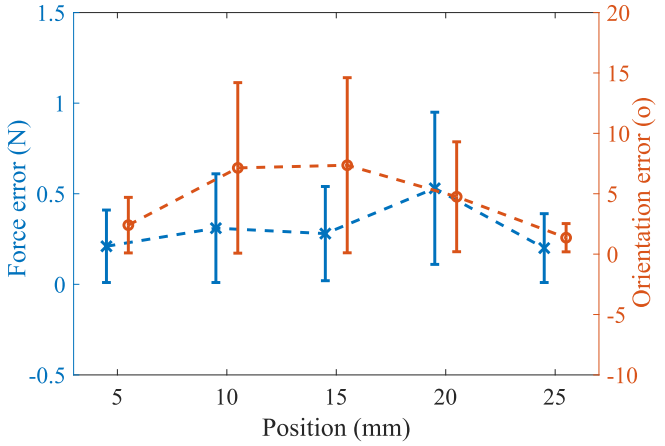

Fig. 14. Average error and standard deviation at different positions for applied force sensing and contact orientation recognition.

To show the advantages of the proposed sensor, we compared the new sensor with the state-of-the-art soft contact force sensor in terms of cost, accuracy, and versatility. Table IV shows that our system is cost-friendly due to the inexpensive material used in this work compared with other costly sensing materials such as silver nanowires [36] and gold [37]. On the other hand, the casting-based fabrication method used in this article is cheaper than those high-resolution printing-based methods [26], [38], and those systems that require embedded electronics [34], [39]. In addition, the sensing accuracy of the new sensor is higher than most other systems. More importantly, the proposed sensor is capable of measuring the force amplitude, contact position, and orientation, which has not been reported in previous studies. The multichannel resistance meter used in this study can quickly respond to the resistance change of liquid metal channels with a high resolution. However, the bench-top meter may have limitations on in situ measuring for industrial scenarios. In practical applications, the resistance measurement circuits can be integrated to monitor the resistance changes. The voltage variations caused by the resistance changes can be measured by multiple analog-to-digital converter (ADC) channels and further processed by embedded controllers. If the number of sensor channels exceeds the number of ADC inputs, a multiplexer (e.g., SparkFun CD74HC4067) could be additionally used for sequential or selective reading of the output of liquid metal channels [40].

The performance of the sensing system can be further improved if it is necessary for some special application scenarios. For example, the position sensing in this article is limited to 1-D. We can extend the positioning range to 2-D by duplicating the existing prototype and laying it out in parallel. Moreover, we can achieve a higher sensing accuracy by measuring the resistance changes in more than three channels. The results in previous sections also indicate that a better perception result can be achieved with a greater difference in geometry between channels. Therefore, we can improve the sensor performance by increasing the dissimilarity between channels. However, due to the fluid characteristics of the liquid metal, it requires a recovery time for the resistance to stabilize. Accordingly, the reported sensor has a limitation in measuring a quick force with a sudden impact of fewer than 0.5 s.

TABLE IV
COMPARISON WITH THE STATE-OF-THE-ART SOFT SENSORS FOR CONTACT FORCE MEASURING

Cost	Sensing mat./dev.	Accuracy(N)	Functions	Ref.
Low	CNT-PDMS-gel	≈ 0.1	For.	[41]
Medium	Pressure sensor	0.56±0.66	For.	[39]
Medium	PDMS-AgNWs	0.11	For.	[36]
High	Galinstan	≈ 0.18	For.	[26], [38]
Low	EGaIn/PDMS	<2	For., Pos.	[32]
Medium	Camera	0.102	For., Ori.	[34]
Medium	FBG	0.94-1.92	For., Ori.	[35]
Low	EGaInSn	0.08-0.25	For., Pos., Ori.	This study

Abbreviation: Sensing mat./dev.: Sensing material/device;
For.: Force, Pos.: position, Ori.: Orientation, Ref.: Reference.

The proposed flexible sensor has significant potential for wearable electronics and human–machine interfaces. For example, the proposed sensor is expected to recognize human fingers' bending joints and bending angles according to the detected force position and force amplitude, respectively. In addition, the proposed sensor can be used as a human–machine interface to control a vehicle, heater, LED, and so on. For example, the touching position can be measured and used to control the turning direction, and the touching force amplitude can be used to control the speed of a vehicle.

VI. CONCLUSION

In this article, we proposed a liquid metal-embedded flexible sensor for the perception of force amplitude, contact position, and orientation. The liquid metal channels are designed with varied cross sections, which results in a gradient resistance along the longitude direction. Thus, the change of resistance is related to both the contact position and contact intensity. We fabricated two prototypes: one with a segmented varied cross section and the other with a continuous gradient cross section. The resistance changes in different channels are collected and analyzed by a neural network. With the AI-based algorithm and novel design, the proposed sensor achieves a high sensing accuracy with sub-Newton force resolution for a wide sensing range (0–20 N). The position error and orientation error are mostly under 2 mm and 5°. Therefore, the proposed flexible sensor has significant potential for a broad range of applications such as human–machine interfaces and wearable electronics.

REFERENCES

[1] T. Kim, S. Lee, T. Hong, G. Shin, T. Kim, and Y.-L. Park, "Heterogeneous sensing in a multifunctional soft sensor for human–robot interfaces," *Sci. Robot.*, vol. 5, no. 49, 2020, Art. no. eabc6878.
[2] B. Aksoy, Y. Hao, G. Grasso, K. M. Digumarti, V. Cacucciolo, and H. Shea, "Shielded soft force sensors," *Nature Commun.*, vol. 13, no. 1, pp. 1–12, 2022.
[3] J. Kim et al., "Wearable smart sensor systems integrated on soft contact lenses for wireless ocular diagnostics," *Nature Commun.*, vol. 8, no. 1, pp. 1–8, 2017.

Authorized licensed use limited to: The University of Hong Kong Libraries. Downloaded on October 05,2024 at 12:00:07 UTC from IEEE Xplore. Restrictions apply.

[4] L. Y. Chen et al., "Continuous wireless pressure monitoring and mapping with ultra-small passive sensors for health monitoring and critical care," *Nature Commun.*, vol. 5, no. 1, pp. 1–10 2014.

[5] Y. Wang, S. Dai, D. Mei, and J. Jin, "A flexible tactile sensor with dual-interlocked structure for broad range force sensing and gaming applications," *IEEE Trans. Instrum. Meas.*, vol. 71, pp. 1–10, 2022.

[6] Y. Yan et al., "Soft magnetic skin for super-resolution tactile sensing with force self-decoupling," *Sci. Robot.*, vol. 6, no. 51, 2021, Art. no. eabc8801.

[7] H. Hu et al., "Wireless flexible magnetic tactile sensor with super-resolution in large-areas," *ACS Nano*, vol. 16, no. 11, pp. 19271–19280, 2022.

[8] K. Park, H. Yuk, M. Yang, J. Cho, H. Lee, and J. Kim, "A biomimetic elastomeric robot skin using electrical impedance and acoustic tomography for tactile sensing," *Sci. Robot.*, vol. 7, no. 67, 2022, Art. no. eabm7187.

[9] S. Niu et al., "A wireless body area sensor network based on stretchable passive tags," *Nature Electron.*, vol. 2, no. 8, pp. 361–368, 2019.

[10] X. Liao, W. Wang, M. Lin, M. Li, H. Wu, and Y. Zheng, "Hierarchically distributed microstructure design of haptic sensors for personalized fingertip mechanosensational manipulation," *Mater. Horizons*, vol. 5, no. 5, pp. 920–931, 2018.

[11] Y. Huang, H. Yuan, W. Kan, X. Guo, C. Liu, and P. Liu, "A flexible three-axial capacitive tactile sensor with multilayered dielectric for artificial skin applications," *Microsyst. Technol.*, vol. 23, no. 6, pp. 1847–1852, 2017.

[12] C. Dagdeviren et al., "Conformable amplified lead zirconate titanate sensors with enhanced piezoelectric response for cutaneous pressure monitoring," *Nature Commun.*, vol. 5, no. 1, pp. 1–10, 2014.

[13] X. Zhao et al., "Self-powered user-interactive electronic skin for programmable touch operation platform," *Sci. Adv.*, vol. 6, no. 28, 2020, Art. no. eaba4294.

[14] S. Qiu, Z. Wang, H. Zhao, and H. Hu, "Using distributed wearable sensors to measure and evaluate human lower limb motions," *IEEE Trans. Instrum. Meas.*, vol. 65, no. 4, pp. 939–950, Apr. 2016.

[15] B. Fang, Z. Xia, F. Sun, Y. Yang, H. Liu, and C. Fang, "Soft magnetic fingertip with particle jamming structure for tactile perception and grasping," *IEEE Trans. Ind. Electron.*, vol. 70, no. 6, pp. 6027–6035, Jun. 2023.

[16] T. Jung and S. Yang, "Highly stable liquid metal-based pressure sensor integrated with a microfluidic channel," *Sensors*, vol. 15, no. 5, pp. 11823–11835, 2015.

[17] D. Wang, J. Guo, C. Sun, M. Xu, and Y. Zhang, "A flexible concept for designing multiaxis force/torque sensors using force closure theorem," *IEEE Trans. Instrum. Meas.*, vol. 62, no. 7, pp. 1951–1959, Jul. 2013.

[18] C. Xiang, C. Liu, C. Hao, Z. Wang, L. Che, and X. Zhou, "A self-powered acceleration sensor with flexible materials based on triboelectric effect," *Nano Energy*, vol. 31, pp. 469–477, Jan. 2017.

[19] S. Joshi, V. D. Bhatt, H. Wu, M. Becherer, and P. Lugli, "Flexible lactate and glucose sensors using electrolyte-gated carbon nanotube field effect transistor for non-invasive real-time monitoring," *IEEE Sensors J.*, vol. 17, no. 14, pp. 4315–4321, Jul. 2017.

[20] J. Kim, Z. Wang, and W. S. Kim, "Stretchable RFID for wireless strain sensing with silver nano ink," *IEEE Sensors J.*, vol. 14, no. 12, pp. 4395–4401, Dec. 2014.

[21] L. Wang, "Potential of using coil-shaped conductive polymer composite to measure temperature and noncontact gap," *IEEE Trans. Instrum. Meas.*, vol. 70, pp. 1–6, 2021.

[22] J. Yan, Y. Lu, G. Chen, M. Yang, and Z. Gu, "Advances in liquid metals for biomedical applications," *Chem. Soc. Rev.*, vol. 47, no. 8, pp. 2518–2533, 2018.

[23] T. Kim, D.-M. Kim, B. J. Lee, and J. Lee, "Soft and deformable sensors based on liquid metals," *Sensors*, vol. 19, no. 19, p. 4250, 2019.

[24] Y. Ren, X. Sun, and J. Liu, "Advances in liquid metal-enabled flexible and wearable sensors," *Micromachines*, vol. 11, no. 2, p. 200, 2020.

[25] Y. Ren, X. Wang, and J. Liu, "Fabrication of high-resolution flexible circuits and sensors based on liquid metal inks by spraying and wiping processing," *IEEE Trans. Biomed. Circuits Syst.*, vol. 13, no. 6, pp. 1545–1551, Aug. 2019.

[26] Y. Wang, Y. Lu, D. Mei, and L. Zhu, "Liquid metal-based wearable tactile sensor for both temperature and contact force sensing," *IEEE Sensors J.*, vol. 21, no. 2, pp. 1694–1703, Aug. 2020.

[27] K. Peng, J. Yao, S. Cho, Y. Cho, H. S. Kim, and J. Park, "Liquid metal embedded real time microfluidic flow pressure monitoring sensor," *Sens. Actuators A, Phys.*, vol. 305, Jan. 2020, Art. no. 111909.

[28] H. An et al., "High-sensitivity liquid-metal-based contact lens sensor for continuous intraocular pressure monitoring," *J. Micromech. Microeng.*, vol. 31, no. 3, 2021, Art. no. 035006.

[29] T. Hu, S. Xuan, L. Ding, and X. Gong, "Liquid metal circuit based magnetoresistive strain sensor with discriminating magnetic and mechanical sensitivity," *Sens. Actuators B, Chem.*, vol. 314, Jul. 2020, Art. no. 128095.

[30] O. G. Akcan, K. Erdil, D. Korkut, E. A. Baran, and Y. D. Gokdel, "Paper-based piezoresistive force encoder for soft robotic applications," *IEEE Sensors J.*, vol. 22, no. 14, pp. 13999–14007, Jul. 2022.

[31] C. Wei et al., "An all-in-one multifunctional touch sensor with carbon-based gradient resistance elements," *Nano-Micro Lett.*, vol. 14, no. 1, pp. 1–18, 2022.

[32] Y. Yang, X. Li, and Y. Shen, "Electrode array-free tactile sensor for addressable force sensing assisted by a neural network," *ACS Appl. Polym. Mater.*, vol. 4, no. 6, pp. 4551–4557, Jun. 2022.

[33] Y. Zhang, A. S. Sezen, and R. Rajamani, "A low-profile supercapacitor-based normal and shear force sensor," *IEEE Sensors J.*, vol. 21, no. 1, pp. 239–249, Jan. 2021.

[34] D. G. Raitt, S.-A. Abad, S. Homer-Vanniasinkam, and H. A. Wurdemann, "Soft, stiffness-controllable sensing tip for on-demand force range adjustment with angled force direction identification," *IEEE Sensors J.*, vol. 22, no. 9, pp. 8418–8427, May 2022.

[35] X. Li, J. Lin, Y. Pang, D. Yang, L. Zhong, and Z. Li, "Three-dimensional force sensor based on fiber Bragg grating for medical puncture robot," *Photonics*, vol. 9, no. 9, p. 630, Sep. 2022.

[36] S. Peng, S. Wu, Y. Yu, B. Xia, N. H. Lovell, and C. H. Wang, "Multimodal capacitive and piezoresistive sensor for simultaneous measurement of multiple forces," *ACS Appl. Mater. Interface*, vol. 12, no. 19, pp. 22179–22190, May 2020.

[37] X. Fu et al., "A high-resolution, ultrabroad-range and sensitive capacitive tactile sensor based on a CNT/PDMS composite for robotic hands," *Nanoscale*, vol. 13, no. 44, pp. 18780–18788, 2021.

[38] Y. Wang, J. Jin, Y. Lu, and D. Mei, "3D printing of liquid metal based tactile sensor for simultaneously sensing of temperature and forces," *Int. J. Smart Nano Mater.*, vol. 12, no. 3, pp. 269–285, Jul. 2021.

[39] L. Lindenroth, D. Stoyanov, K. Rhode, and H. Liu, "Toward intrinsic force sensing and control in parallel soft robots," *IEEE/ASME Trans. Mechatronics*, vol. 28, no. 1, pp. 80–91, Feb. 2023.

[40] H. Shi, I. Gonzalez-Afanador, C. Holbrook, N. Sepulveda, and X. Tan, "Soft pressure sensor for underwater sea lamprey detection," *IEEE Sensors J.*, vol. 22, no. 10, pp. 9932–9944, May 2022.

[41] M. H. Rosle, Z. Wang, M. N. I. Shiblee, K. Ahmed, H. Furukawa, and S. Hirai, "Soft resistive tactile sensor based on CNT-PDMS-Gel to estimate contact force," *IEEE Sensors Lett.*, vol. 6, no. 3, pp. 1–4, Mar. 2022.

Min Wang (Graduate Student Member, IEEE) received the B.S. degree from the Hefei University of Technology (HFUT), Hefei, China, in 2017, and the M.S. degree from the Harbin Institute of Technology Shenzhen (HITSZ), Shenzhen, China, in 2020. He is currently pursuing the Ph.D. degree with the City University of Hong Kong, Hong Kong, SAR, China.

His main research interests include actuation and perception for soft and microrobots.

Jingjing Zhang received the B.S. degree in mechanical engineering from the Kunming University of Science and Technology, Kunming, China, in 2021, and the M.S. degree in mechanical engineering from the City University of Hongkong, Hongkong, China, in 2022.

Her research interest is soft sensing systems.

Authorized licensed use limited to: The University of Hong Kong Libraries. Downloaded on October 05,2024 at 12:00:07 UTC from IEEE Xplore. Restrictions apply.

Ruomao Liu received the B.S. degree from Shenzhen University, Shenzhen, China, in 2021, and the MSC degree from the City University of Hong Kong, Hong Kong, SAR, China, in 2022.

He is currently a Research Assistant with the Biorobot Laboratory, City University of Hong Kong. His main research interests are in soft robotics and magnetic control.

Tianyi Wu received the B.S. and M.S. degrees in mechanical engineering from the Beijing Institute of Technology, Beijing, China, in 2017 and 2020, respectively. He is currently pursuing the Ph.D. degree in mechanical engineering with the City University of Hong Kong, Hong Kong, SAR, China.

His current research interests include deep learning, machine vision, and assembly automation.

Wei Dai received the B.Eng. degree from the School of Mechanical and Automotive Engineering, South China University of Technology, Guangzhou, China, in 2021. He is currently pursuing the Ph.D. degree with the Department of Mechanical Engineering, City University of Hong Kong, Hong Kong, SAR, China.

He was a Visiting Student at the University of St Andrews, St Andrews, Scotland, in 2019. Currently, he is dedicated to self-supervised learning and domain adaptation. His current research interests include medical image analysis and label-efficient learning.

Rui Liu received the B.S. degree from Central South University, Changsha, China, in 2013, and the M.S. degree from Zhejiang University, Hangzhou, China, in 2016. He is currently pursuing the Ph.D. degree with the City University of Hong Kong, Hong Kong, SAR, China.

His main research interest is robotics and automation.

Jiachen Zhang (Member, IEEE) received the Ph.D. degree from the University of Toronto, Toronto, ON, Canada, in 2018.

From 2019 to 2021, he worked as a Guest Scientist and a Humboldt Research Fellow with the Physical Intelligence Department, Max Planck Institute in Germany, Munich, Germany. In the summer of 2021, he joined the Department of Biomedical Engineering, City University of Hong Kong, Hong Kong, SAR, China, as an Assistant Professor. His research focuses on the applications of small-scale robotics to minimally invasive or noninvasive healthcare. He explores the methodology of using a magnetic field and smart materials to achieve multifunctional robotic systems across different size scales.

Jun Liu (Member, IEEE) received the Ph.D. degree from the University of Toronto, Toronto, ON, Canada, in 2016.

From 2017 to 2019, he worked as a Postdoctoral Fellow with Weill Cornell Medical College, Cornell University, Ithaca, NY, USA. He is currently an Assistant Professor with the Department of Mechanical Engineering, City University of Hong Kong, Hong Kong, SAR, China. His current research interests include micro–nanorobotics, medical robotics, and smart sensors and actuators.

Dr. Liu research has been recognized in the field of robotics and automation by winning multiple awards, including the Best Student Paper Award and the Best Medical Robotics Paper Finalist Award from the IEEE International Conference on Robotics and Automation in 2014 and the IEEE TRANSACTIONS ON AUTOMATION SCIENCE AND ENGINEERING Best New Application Paper Award in 2018.

Authorized licensed use limited to: The University of Hong Kong Libraries. Downloaded on October 05,2024 at 12:00:07 UTC from IEEE Xplore. Restrictions apply.